

attributable in part to the lack of tropical cyclones impacting the region, as well as the emergence of El Niño late in the year.

- South America: The overall weather conditions varied from very wet to very dry. However, the year was warm throughout most of the continent. Classical ENSO teleconnections, as well as modulation by the MJO, were observed.
- Asia: Russian temperatures were anomalously warm, especially in December when records were broken, including in Moscow. However, January was very cold across the country. China experienced its warmest year on record and rainfall deficits. The Indian monsoon onset commenced in the fourth pentad in May. Heat waves struck parts of South Asia in May and June.
- Europe: Europe was unusually warm, with new high-temperature records set in many countries. A summer heat wave and a very warm autumn contributed to this warmth.
- Oceania: Parts of Australia were the warmest on record. Many locations were impacted by severe drought and tropical cyclones, including TC Larry, which was one of the strongest storms to hit Australia in decades.

2. GLOBAL CLIMATE—A. Horvitz, Ed.

a. Overview—A. Horvitz

Anomalous warmth continued at the surface and throughout the troposphere in 2006. The global annual average surface temperature in 2006 ranked as either the fifth or sixth highest, depending on the dataset used. Worldwide, land surface temperatures ranked as fourth highest on record according to NOAA/NCDC, and SSTs ranked as the fifth highest. The annual global mean low- to midtroposphere anomaly for 2006 was the third to fifth warmest (depending on the dataset) since records began in 1958.

Global land surface precipitation was above average in 2006 with an annual anomaly 34.0 mm (3.0%) above the 1961–90 mean. Over the tropical Pacific, weak El Niño conditions developed during mid-2006 and lasted through the rest of the year. However, the coupling between the warmer-than-normal SST and the atmosphere did not materialize fully and no discernable ENSO signature was evident in the precipitation anomaly pattern. The 12-month running means of NH snowfall extent were below the long-term average throughout the year, continuing the trend since the late 1980s. The preliminary globally averaged atmospheric CO₂ mole fraction in 2006 was approximately 2.3 ppm greater than the 2005 global annual mean.

New to 2006, this section also provides a summary for global cloudiness, aerosols, and global winds. Also included is a report on teleconnection patterns and blocking reflecting large-scale changes in the atmospheric wave and jet stream patterns, which influence temperature, rainfall, storm tracks, and jet stream location and intensity over vast distances.

b. Global temperature

1) SURFACE TEMPERATURE—M. J. Menne and T. C. Peterson

The global annual average surface temperature in 2006 ranks as either the fifth or sixth highest according to analysis conducted independently at institutions in the United States and United Kingdom. As shown in Fig. 2.1, the global value for 2006 ranks as the fifth highest on record according to NOAA/NCDC and NASA's GISS, and as the sixth highest according to the University of East Anglia Climate Research Unit (CRU)/Met Office (MO) Hadley Centre estimate. Calculated as a linear trend, the rates of temperature change since 1901 are 0.064°, 0.066°, and 0.073°C decade⁻¹ for the NOAA/NCDC, NASA GISS, and CRU/MO analyses, respectively. However, the temperature change is not linear, and the rise from 1979 to 2006 is approximately 0.17°C decade⁻¹ according to all three sources (Fig. 2.2).

All three global temperature analyses combine air temperature data over land with SST. The NOAA/NCDC surface temperature analysis is described in Smith and Reynolds (2005), the NASA GISS analysis is described in Hansen et al. (2001), and the CRU/MO (HadCRUT3) analysis is described in Brohan et al. (2006). Because the analyses make use of different data reconstruction and interpolation approaches, they differ most in regions with sparse data. Where data are plentiful and for global averages the three

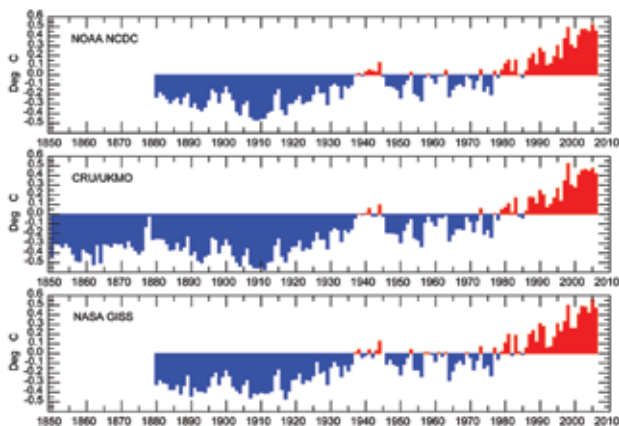


FIG. 2.1. Annual global surface temperature departures from the 1961–90 average. [Source: NOAA/NCDC, CRUHadCRUT3, and NASA GISS.]

analyses agree well with each other and with the other historical “global” temperature time series shown in Fig. 2.3. While the underlying data sources for all the time series differ widely, the high degree of trend consistency among them, since 1901, increases the confidence that the changes they depict are robust (Sommerville et al. 2007).

Worldwide, surface air temperatures over land rank as the fourth highest on record according to the NOAA/NCDC record, and SSTs ranked as the fifth highest (not shown). Warming has occurred in both land temperatures and SST. As might be expected given the heat capacity of oceans, land temperatures have risen at over twice the ocean rate since 1979 (about $0.30^{\circ}\text{C decade}^{-1}$ versus $0.12^{\circ}\text{C decade}^{-1}$).

The geographic distribution of annual temperature anomalies is shown in Fig. 2.4. Regionally, 2006 temperatures were the highest or near highest on record in the United States, Canada, China, the United Kingdom, Spain, and the Netherlands, as well as parts of Australia. These events are discussed in detail in the regional climate sections (see section 6).

2) UPPER-AIR TROPOSPHERIC TEMPERATURES—J. C. Christy

The temperature variations of three broad atmospheric layers, the low to midtroposphere (LT; surface to 300 hPa), the midtroposphere to lower stratosphere (MT; surface to 70 hPa), and the upper troposphere to lower stratosphere (LS; 150–20 hPa) are monitored by two observing systems—radiosondes and satellites. Three radiosonde-based products are available—HadAT2 (Thorne et al. 2005), based on about 650 stations; RATPAC (Free et al. 2005), based on 85 stations; and RAOBCORE (version 1.4; Haimberger 2007), based on about 1100 stations. Satellite products for LT, MT, and LS are from the UAH (Christy et al. 2003; Spencer et al. 2006; version 5.2 LT, version 5.1

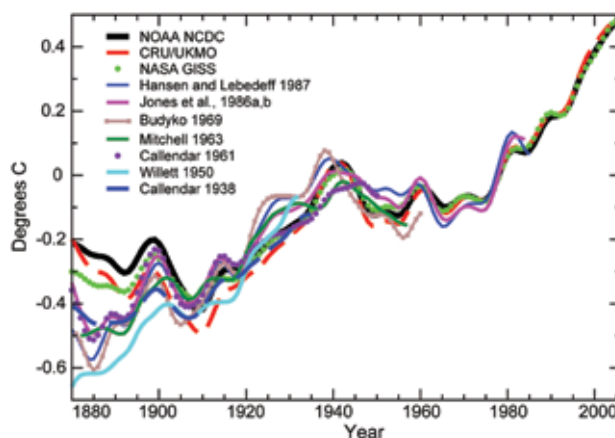


FIG. 2.3. “Global” temperature time series: Callendar (1938): global—based on land stations; Willett (1950): global—based on land stations; Callendar (1961): 60°N to 60°S—based on land stations; Mitchell (1963): global—based on land stations; Budyko (1969): Northern Hemisphere—based on land stations and ship reports; Jones et al. (1986a,b): global—based on land stations; Hansen and Lebedeff (1987): global—based on land stations. The NOAA/NCDC, CRU/MO, and NASA GISS time series are expressed as anomalies from the 1961–90 mean ($^{\circ}\text{C}$). Each of the other time series was originally presented as anomalies from the mean temperature of a specific, but differing base period. To make them comparable, the historic time series have been adjusted such that the mean of their last 30 yr is identical to the equivalent period in the NOAA/NCDC anomaly time series. All series have been smoothed using a 13-point filter.

MT; and LS) and RSS (Mears et al. 2003; Mears and Wentz 2005; version 3.0). An MT dataset from UMD (Vinnikov et al. 2006) is also included. “Annual” is defined as the period from December through November (otherwise known as the meteorological year).

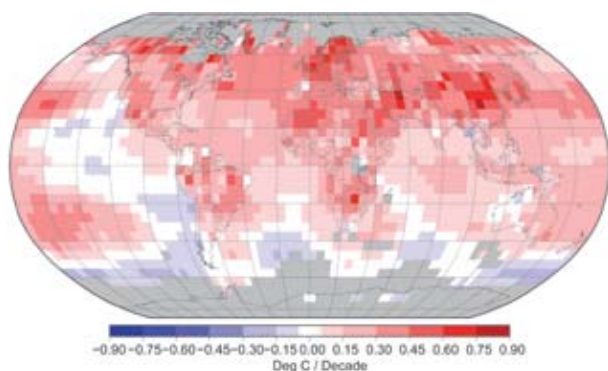


FIG. 2.2. Pattern of linear surface temperature trends 1979–2006 according to the NOAA/NCDC analysis. Gray areas indicate data-sparse regions.

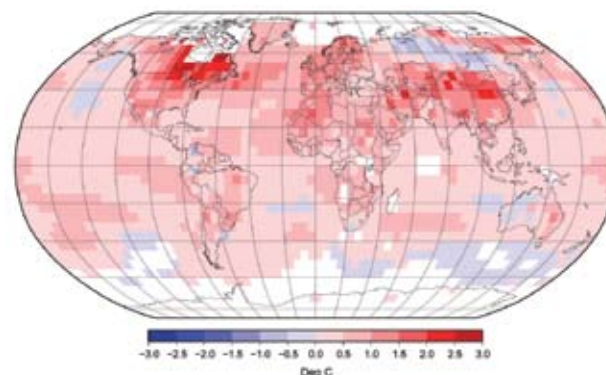


FIG. 2.4. Geographic distribution of temperature anomalies in 2006. Departure from the 1961–90 average. [Source: NOAA/NCDC.]

TABLE 1. Linear trends ($^{\circ}\text{C decade}^{-1}$) of global and tropical (20°S – 20°N) anomalies for 1958–2006. In parentheses are trends for 1979–2006.

| | HadAT2 ¹ | RATPAC ¹ | RAOBCORE ¹ | UAH ³ | RSS ³ | UMd ^{3,4} |
|-------------|---------------------|---|-----------------------|------------------|------------------|--------------------|
| Global LT | +0.15(+0.17) | +0.15 (+0.16) | +0.14(+0.16) | (+0.14) | (+0.19) | |
| Tropical LT | +0.12 (+0.09) | +0.14 (+0.12) | +0.13 (+0.12) | (+0.08) | (+0.18) | |
| Global MT | +0.09 (+0.07) | +0.08 (+0.04) | +0.10 (+0.12) | (+0.05) | (+0.13) | (+0.21) |
| Tropical MT | +0.09 (+0.02) | +0.08 (+0.03) | +0.13 (+0.12) | (+0.06) | (+0.14) | (+0.21) |
| Global LS | –0.35 (–0.54) | –0.43 ² (–0.70) ² | –0.30 (–0.40) | (–0.44) | (–0.32) | |
| Tropical LS | –0.34 (–0.55) | –0.50 ² (–0.72) ² | –0.24 (–0.34) | (–0.38) | (–0.31) | |

¹ Radiosonde datasets are characterized by more limited coverage with few data south of 50°S latitude and little in oceanic areas.

² The use of the 100–50-hPa layer as an approximation for the satellite LS layer leads to slightly more negative trends because the temperature trend below 100 hPa, which makes up a portion of the LS signal, is positive but not included in the 100–50-hPa layer.

³ UAH coverage is 85°S – 85°N , RSS 70°S – 85°N . UMd MT covers 82.5°S – 82.5°N . Since less warming has been observed in the high southern latitudes, their inclusion tends to reduce “global” trends, for example, the UAH “global” LT trend is $0.02^{\circ}\text{C decade}^{-1}$ more positive if limited to 50°S – 85°N .

⁴ Through 2005 only.

The annual global mean LT anomaly for 2006 was the third to fifth warmest among the datasets since records began in 1958 (Fig. 2.5), about 0.2°C cooler than the warmest year of 1998. All datasets are consistent with global trend values of $+0.16 \pm 0.03^{\circ}\text{C decade}^{-1}$ since 1979 and $+0.14 \pm 0.01^{\circ}\text{C decade}^{-1}$ since 1958 (Table 1). Note that the datasets are constructed using independently developed methodologies. Because none of these datasets claim precision better than $\pm 0.05^{\circ}\text{C decade}^{-1}$, this level of agreement is very encouraging, providing a relatively confident assessment of global LT trends.

A more visual interpretation of long-term change suggests a relatively large increase in global temperatures around 1977 and another shift to warmer temperatures associated with the 1997/98 ENSO (Seidel and Lanzante 2004). Since 1977 no seasonal anomaly has dipped below -0.4°C , and since 2000 none has dipped below the 1979/88 mean.

Regionally, the largest 2006 positive anomaly magnitudes occurred in the Arctic (not shown), where the most positive trends since 1979 are also found, because both UAH and RSS measure a trend greater than $+0.4^{\circ}\text{C decade}^{-1}$ poleward of 60°N .

A similar picture is indicated for the MT layer (not shown), which includes some stratospheric influence. The rankings for 2006 place it from the third to the ninth warmest among the datasets; however, the magnitude of the temperature differences in this

range is not significant. Linear trends are more negative than for the LT layer because of the influence of the cooling stratosphere (Table 1).

The QBO shifted to the westerly or warm phase in 2006 and thus, tropical stratospheric temperatures (LS) were warmer than those in 2005 by about $+0.6^{\circ}\text{C}$. Globally, the 2006 annual anomaly ranked from being the coldest to the seventh coldest, with both satellite datasets ranking 2006 as the second coldest. In particular, the south polar region was exceptionally

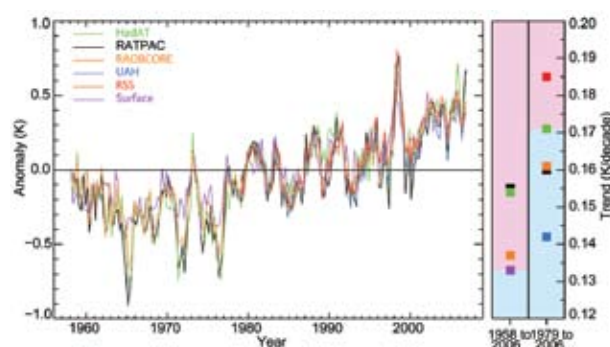


FIG. 2.5. Time series of seasonal anomalies of the LT, with respect to 1979–88. Trend values for two periods, beginning in 1958 and in 1979, are plotted on the right. The background color of the right panels indicates the LT trend relative to the surface trend (HadCRUT3) as being more positive (lavender) or negative (light blue). [Source: H. Tichner, Hadley Centre.]

cold in autumn (SON) 2006, countering a series of recent warm temperatures for that season (see 2005 report). Linear trends are more variable among the datasets and indicate that considerably more analysis is needed to understand the differences and give better estimates of confidence. Even so, all indicate significant cooling over the period (Table 1), though since about 1995 the global trends have not been remarkable (Fig. 2.6).

c. Hydrologic cycle

1) GLOBAL PRECIPITATION

(i) Over land—J. H. Lawrimore and D. H. Levinson

Global precipitation anomalies determined from land-based gauges were analyzed on both an annual and a seasonal basis using data from the GHCN (Peterson and Vose 1997). Anomalies from 1900 to 2006 were determined from the GHCN dataset with respect to the 1961–90 mean using those stations with a minimum of 25 years of data during the 30-year base period (Vose et al. 1992). Highlights of selected regional precipitation anomalies are also included below, with additional regional details provided in section 6.

Global land surface precipitation was above average in 2006, with an annual anomaly that was 34.0 mm (3.0%) above the 1961–90 mean (Fig. 2.7a). It was the most anomalously wet year since 2000, and the eighth wettest year since reliable global records began in 1900. On a seasonal basis only JJA was drier than average. It was the fourth wettest DJF and the second wettest boreal spring (MAM) on record (Figs. 2.7b and 2.7c, respectively). The DJF and MAM anomalies were +16.7 (+6.5%) and +13.9 (+4.7%) mm, respectively.

Precipitation patterns consistent with the presence of La Niña conditions in early 2006 were evident in

some areas of the world (Ropelewski and Halpert 1987). In January, above-normal precipitation occurred in much of the Maritime Continent, northern Australia, and western Pacific. Precipitation was also above average in parts of southern Africa. Also consistent with La Niña was above-average winter rain and snowfall in the northwestern United States, while precipitation and snowpack in the southwest United States were at near-record to record low levels. In April, enhanced rainfall persisted in the western equatorial Pacific from Queensland, Australia, through much of Indonesia, even as the weak La Niña episode ended. Additional details on ENSO conditions are available in section 4b.

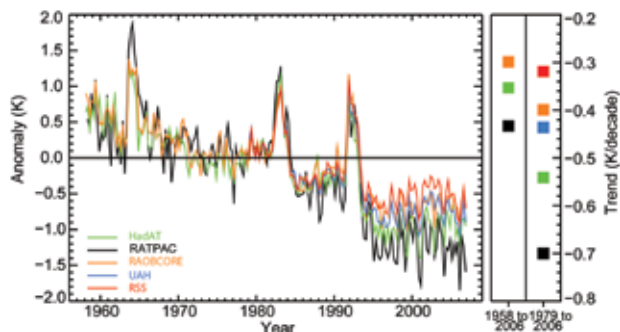


FIG. 2.6. As in Fig. 2.5, but for the LS, and no surface comparison. Warming events follow major volcanic eruptions: Agung (1963), El Chichón (1982), and Mt. Pinatubo (1991). [Source: H. Tichner, Hadley Centre.]

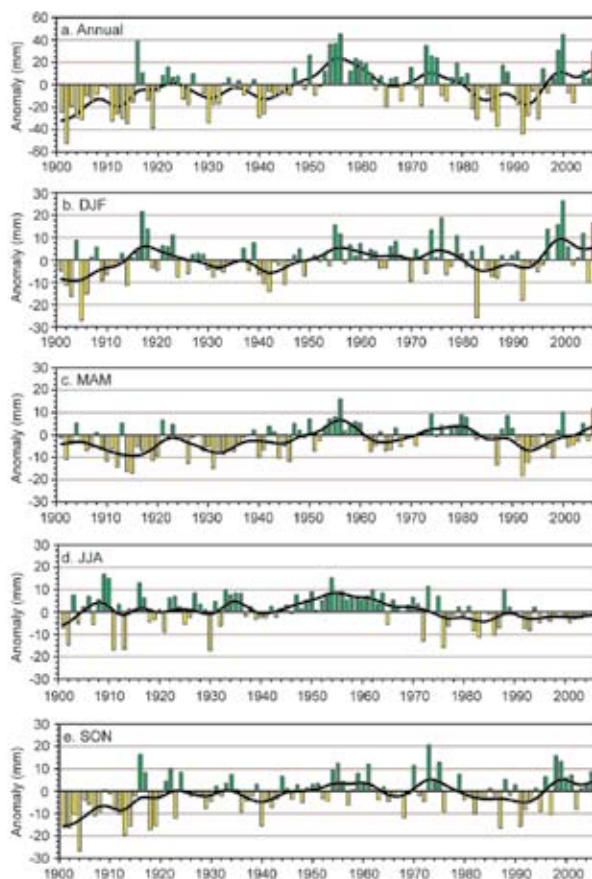


FIG. 2.7. Time series of annual and seasonal global land surface precipitation anomalies over the period 1900–2006, based on observations from the Global Historical Climatology Network dataset (Vose et al. 1992): (a) annual, (b) December 2005–February 2006, (c) March–May, (d) June–August, and (e) September–November. The precipitation anomalies were calculated (mm) with respect to the 1961–90 base period mean: green bars = positive anomalies, yellow bars = negative anomalies, and red bar = 2006 anomaly. In addition, the black line in each time series denotes the smoothed annual or seasonal values using a 13-point binomial filter.

Precipitation during JJA was 2.4 mm (0.6%) below average, which is a drier-than-average pattern that has occurred in all but 8 of the past 30 such seasons (Fig. 2.7d). The southwest monsoon season was near average in total rainfall on the Indian subcontinent, but periods of heavy rain resulted in record 24-h rainfall totals in some locations. Heavy rains also fell in parts of Africa. In much of Niger, the heaviest rainfall in decades led to significant agricultural losses with tens of thousands of people affected in August. Heavy rain also caused devastating floods in Ethiopia in the same month (see section 6b).

While JJA has largely been drier than average in recent decades, much of the past decade has been wetter than average during SON, and 2006 was no exception (Fig. 2.7e). Precipitation was 7.7 mm (2.4%) above average, making this the 8th out of the past 10 SONs that were wetter than average for the globe. A long-lasting drought in the Greater Horn of Africa ended with heavy rainfall and reports of the worst flooding in 50 years from October through early December. The worst-hit areas were in Ethiopia, Kenya, and Somalia, where some stations received more than six times their average monthly rainfall.

Conversely, severe drought continued in eastern Australia in late 2006, as the rapid onset of El Niño conditions in late August and September exacerbated unusually dry conditions that had been present throughout much of the year. For many areas of Australia, the lack of adequate rainfall in 2006 compounded longer-term dry conditions, with large regions not having yet recovered from the droughts of 2002/03 and 1997/98 (Nicholls 2004). Dry conditions have now persisted for 5–10 years in many areas, and for almost three decades in southwestern portions of western Australia.

Other areas of the world also have had an increasing incidence of drought over the past three decades. The percentage of the world affected by severe drought more than doubled from approximately 10%–15% in the early 1970s to approximately 30% by 2002 (Dai et al. 2004). Almost half of this increase has been linked to rising surface temperatures. The increase in global surface temperature of near 0.18°C decade⁻¹ since the mid-1970s (section 2bi) is thought to have increased the evaporation of moisture from many land areas. One significant consequence has been that even though decreasing trends in precipitation at regional scales were a factor associated with increasing drought coverage in some areas, the increase in areas affected by severe drought occurred even while precipitation increased in most regions of the world (Dai et al. 2004).

For global land areas as a whole, total annual precipitation increased at a rate of 0.59% decade⁻¹ since the mid-1970s and 0.19% decade⁻¹ since the start of the twentieth century. The largest increases have been in the high latitudes of the NH. Although there has been large decadal variability and periods of decreasing precipitation trends during the past century, the monotonic trend averaged within the 55°–85°N latitude band from 1900 to 2006 was approximately +1.2% decade⁻¹. During the same period precipitation increased at a rate of 0.4% decade⁻¹ in the midlatitudes of the NH (30°–55°N) and 0.25% decade⁻¹ in the midlatitudes of the Southern Hemisphere. A decreasing trend near 0.4% decade⁻¹ occurred from 10° to 30°N. This in part reflected large negative trends over western and eastern Africa, where rainfall decreased at a rate near 0.8% decade⁻¹.

(ii) *Precipitation over oceans*—P. Xie and J. E. Janowiak

Real-time monitoring of global oceanic precipitation is conducted at NOAA's Climate Prediction Center (CPC) using the "CAMS-OPI" dataset (Janowiak and Xie 1999). By combining the gauge observations of precipitation collected and archived by CPC via the CAMS (Ropelewski et al. 1985) with the satellite-based OPI (Xie and Arkin 1998), the CAMS-OPI database provides monthly precipitation estimates over global land and ocean. Several large-scale anomalies, discussed below, were observed in 2006 (Fig. 2.8, bottom panel).

The mean precipitation amount over the entire global oceans during 2006 was 2.812 mm day⁻¹, which is equivalent to a freshwater influx of 1026.4 kg m⁻². Maximum annual precipitation rates of over 9 mm day⁻¹ were observed over the tropical western Pacific where the ITCZ merges with the SPCZ (near the equator and 150°E). Relatively light precipitation was recorded over the oceanic dry zones in the southeast Pacific, the northeast Pacific off the coast of the southwestern United States, the southeast Atlantic, the tropical North Atlantic near western Africa, and the southeastern Indian Ocean.

Over the tropical Pacific, weak (and at times moderate) El Niño conditions developed during mid-2006 and lasted through the rest of the year. However, coupling between the warmer-than-normal SST (see section 3b) and the atmosphere did not materialize fully, and no discernable ENSO signature was seen in the precipitation anomaly pattern. In fact, the precipitation pattern in the tropical Pacific was more characteristic of La Niña conditions. These include greater-than-normal rainfall east of the Maritime Continent and over the ITCZ and SPCZ, and less-

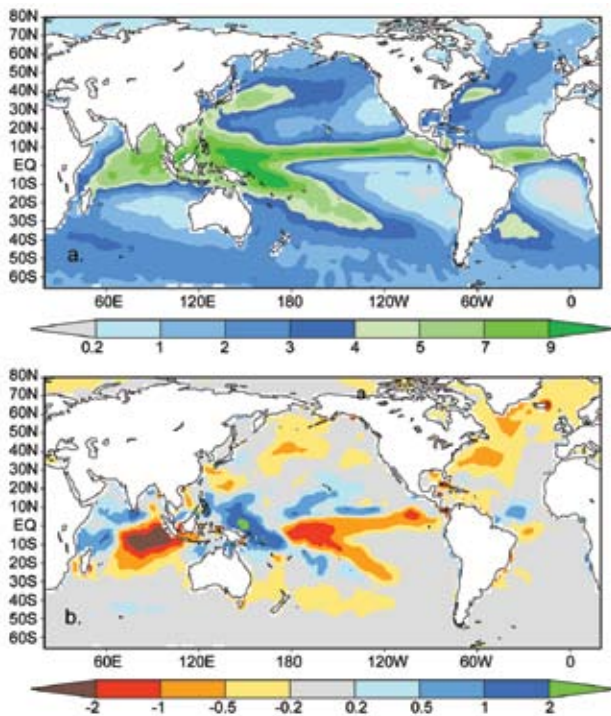


FIG. 2.8. Annual mean total precipitation (mm day^{-1} , upper) and annual mean precipitation anomaly [mm day^{-1} , bottom] for 2006 as observed by the gauge-satellite merged dataset of CAMS-OPI (Janowiak and Xie 1999). Precipitation anomalies were calculated using 1979–95 as the base period.

than-normal rainfall over much of the central and eastern near-equatorial Pacific (Fig. 2.8). In contrast, a time-longitude diagram of near-equatorial precipitation anomalies (Fig. 2.9) showed a steady eastward progression of positive rainfall anomalies beginning in June 2006 that coincided with the developing El Niño conditions. However, the eastward movement was restricted to the area from 160°E to about 170°W .

Over the Indian Ocean, the precipitation distribution during 2006 was characterized by a large negative anomaly over the eastern portion of the basin between the equator and 20°S . This anomaly was associated with a cold water mass that developed during the second half of the year. In contrast, the western portion of the Indian Ocean experienced wetter-than-normal conditions that included the entire Arabian Sea southward to Madagascar. This anomaly pattern is indicative of the positive phase of the Indian Ocean dipole pattern (Baquero-Bernal et al. 2002).

The lower-than-normal rainfall over the Caribbean Sea and the Gulf of Mexico (Fig. 2.8) may have been associated with the relatively inactive hurricane season. Elsewhere, weak negative precipitation

anomalies were observed over the northwestern Atlantic Ocean during most of 2006.

2) SNOW—D. A. Robinson

Annual SCE over NH lands averaged 24.9 million km^2 in 2006; this is 0.6 million km^2 less than the 37-yr average and ranks 2006 as having the 27th most extensive cover of record. This evaluation considers snow over the continents, including the Greenland ice sheet. The SCE in 2006 ranged from 47.7 million km^2 in January to 2.2 million km^2 in August. Monthly snow extent values are calculated at the Rutgers–The State University of New Jersey Global Snow Laboratory from weekly SCE maps produced by NOAA meteorologists, who rely primarily on daily visible satellite imagery to construct the maps.

Hemispheric SCE was above the long-term mean in January, February, and October, but close to or below the mean in all other months. Thus, the 12-month running means of NH extent were below the long-term average throughout the year (Fig. 2.10). This has almost exclusively been the situation since the late 1980s. Eurasian SCE was somewhat above the long-term average in 2006 and ranked as the 17th

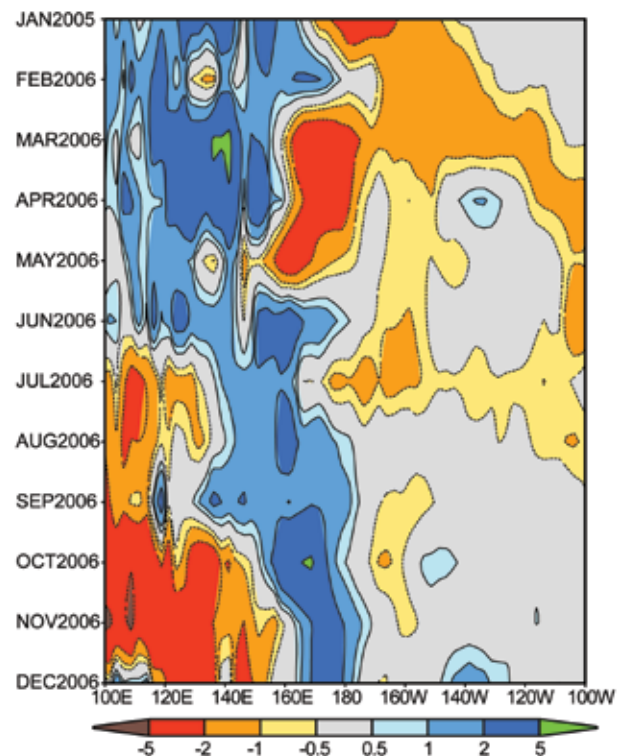


FIG. 2.9. Time-longitude section of precipitation anomaly averaged over the tropical Pacific (10°S – 10°N) as observed by the CAMS-OPI (Janowiak and Xie 1999). Precipitation anomalies were calculated using 1979–95 as the base period.

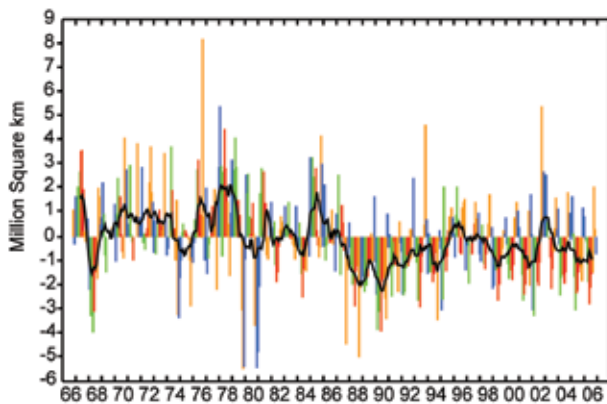


FIG. 2.10. Anomalies of monthly snow cover extent over Northern Hemisphere lands (including Greenland) between November 1966 and December 2006. Also shown are 12-month running anomalies of hemispheric snow extent, plotted on the seventh month of a given interval. Anomalies are calculated from NOAA snow maps. Mean hemispheric snow extent is 25.5 million km² for the full period of record. Monthly means for the period of record are used for nine missing months between 1968 and 1971 in order to create a continuous series of running means. Missing months fall between June and October; no winter months are missing.

most extensive cover of the satellite era. North American SCE was much below average, ranking 36th, the second least extensive.

As is common, 2006 SCE showed significant variability on temporal and spatial scales. For instance, hemispheric SCE ranked in the top 10 in January and October, while totals ranked in the lowest 10 from May through September, as well as in December. January's anomaly was positive as a result of Eurasian extent being the second largest of record, despite North America ranking 39th, or second least extensive. October's high ranking was the result of extensive cover over both continents, following a late spring, summer, and early fall, when both continents ranked quite low. Spring and summer snow cover continues to be less extensive in the second half of the satellite record than in the first half (Fig. 2.11). Lower-than-average North American SCE was first noted in North America in April,

while it was not until June that Eurasian cover fell to well below average extent. Fall and winter SCE continue to show considerable year-to-year variability, however there are no apparent trends.

Over the contiguous United States, January SCE was the second lowest on record, while April and November ranked in the top 10 lowest. Meanwhile, October SCE was the 14th largest. Alaskan cover ran close to average from January through summer's end, and then fell well below average during the fall.

3) CLOUDINESS—A. Heidinger, A. Evan, and B. Baum

Cloudiness in 2006 was dominated by La Niña at the beginning of 2006, and by El Niño at the end of the year. The dataset used in this analysis of global cloudiness is based on 25 years of data (1982–present) from the series of AVHRR imagers on the NOAA polar-orbiting platforms, and is known as the AVHRR PATMOS-x (information available online at <http://cimss.ssec.wisc.edu/clavr/patmosx.html>).

Figure 2.12 is a map of boreal winter cloudiness (January–March) for 2006 in which the climatological mean based on the PATMOS-x record for the same months has been subtracted. Inspection of this figure shows that the enhanced Pacific trade flow results in a reduction in cloudiness across the equatorial eastern Pacific that is caused by cooler-than-normal SSTs. Also present is an increase in cloud amount in the Indonesian region, consistent with the characteristic warming of ocean temperatures that occurs during a La Niña event. A slight cooling across the Indian

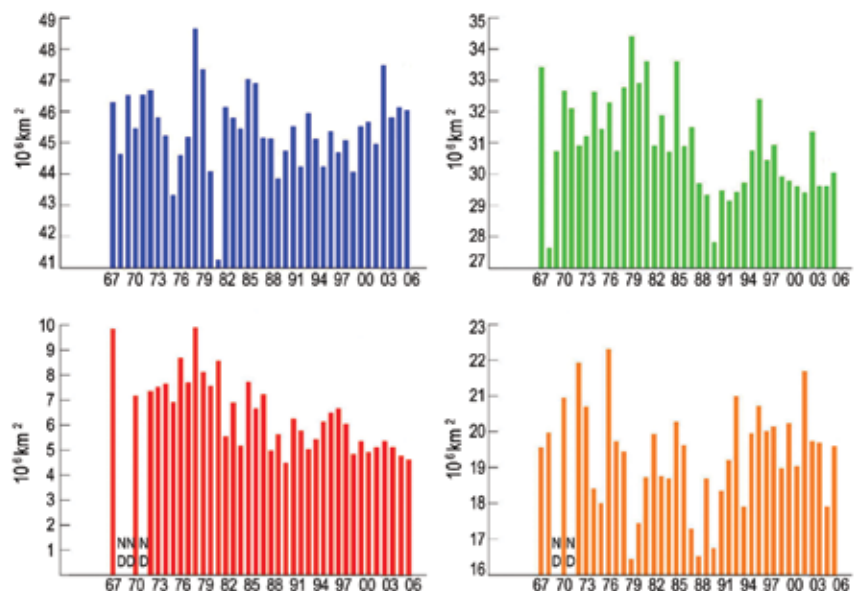


FIG. 2.11. Seasonal snow cover extent over Northern Hemisphere lands (including Greenland) between winter (December–February) 1966–67 and fall (September–November) 2006. Calculated from NOAA snow maps.

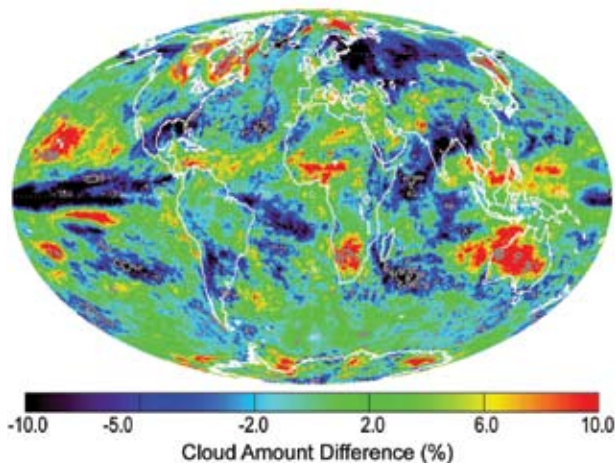


FIG. 2.12. Map of boreal winter (January–March) absolute cloud amount differences (%) between the observations in 2006 and the climatological winter mean based on the period from 1982 to 2006.

Ocean and the observed reduction in cloud amounts during this period is also consistent with the negative phase of an ENSO period.

Figure 2.13 provides similar analysis, but for the boreal fall of 2006, consisting of the cloud amount for October, November, and December. There is a sharp reversal of cloud patterns across the equatorial Pacific associated with the onset of an El Niño event. The easing of the easterly trade flow and the subsequent eastward migration of warmer sea surface temperatures results in the pattern of increased cloudiness along the eastern equatorial Pacific, a

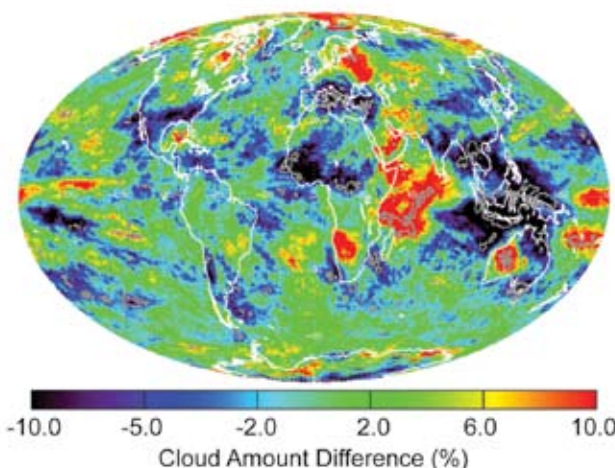


FIG. 2.13. Map of boreal fall cloudiness (October–December) absolute cloud amount differences (%) between the observations in 2006 and the climatological mean for the boreal fall based on the period from 1982 to 2006. The data are provided by the AVHRR PATMOS-x project.

drastic decrease in cloudiness from northern Australia to Southeast Asia, and an increase in cloudiness across the Indian Ocean. While the departure from the mean state is more than a 10% reduction in cloudiness in these regions, this anomaly (and that of the La Niña state) is not statistically significant at the 95% confidence level, and is by no means impressive when compared to cloud amount anomalies during much stronger ENSO events.

The year 2006 also featured an increase in high-level cloudiness across much of southern Africa. This anomaly was more prevalent and statistically significant in a map of annual mean high cloud anomalies (Fig. 2.14). These anomalies in high cloud amounts are consistent with a strong monsoon observed toward the beginning of 2006 that stretched across the region.

d. Trace gases and aerosols

1) CARBON DIOXIDE—E. J. Dlugokencky and R. C. Schnell

The CO₂ emitted from fossil fuel burning is partitioned into the following three mobile reservoirs: atmosphere, oceans, and terrestrial biosphere. One result of fossil fuel combustion has been that atmospheric CO₂ has increased from about 280 ppm at the start of the industrial revolution to more than 380 ppm today. Roughly half of the emitted CO₂ remains in the atmosphere and the remainder has gone into the following two sinks: oceans and the land biosphere (which includes plants and soil carbon).

Currently, more than 7 Pg (Pg = 10¹⁵ g) of carbon is emitted into the atmosphere by fossil fuel combus-

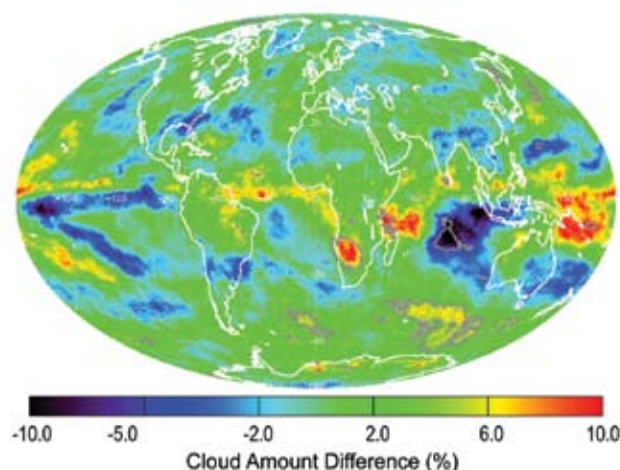


FIG. 2.14. Difference (%) between the mean 2006 high cloud amounts and the climatological mean high cloud amounts (1982–2006). There are regions where the anomaly is a statistically significant departure from the mean state, notably in the Indian Ocean and over South Africa.

tion each year. During the 1990s, net uptake by the oceans was estimated as $1.7 \pm 0.5 \text{ Pg yr}^{-1}$ and by the land biosphere as $1.4 \pm 0.7 \text{ Pg yr}^{-1}$ (Prentice et al. 2001). The gross fluxes between the atmosphere and oceans, and the atmosphere and terrestrial biosphere (photosynthesis and respiration), are on the order of 100 Pg yr^{-1} . Interannual variations in the atmospheric increase of CO_2 (see Fig. 2.15, based on Conway et al. 1994) are because of small changes in these net fluxes, not because of variations in fossil fuel emissions. Most attempts to explain the interannual variability of the atmospheric CO_2 increase have focused on short-term climate fluctuations (e.g., ENSO and post-Mt. Pinatubo cooling), but the mechanisms, especially the role of the terrestrial biosphere, are not well understood. To date, about 5% of conventional fossil fuels have been combusted. If combustion were stopped today, after a few hundred years, 15% of the total carbon emitted would remain in the atmosphere and the remainder would be in the oceans.

The preliminary globally averaged atmospheric CO_2 mole fraction in 2006 was 381.1 ppm, which is $\sim 2.3 \text{ ppm}$ greater than the 2005 global annual mean. While there has been an average annual increase of 1.6 ppm yr^{-1} since 1980, the average rate of increase since 2000 has been 2.1 ppm yr^{-1} . This suggests that the fraction of CO_2 emitted from fossil fuel combustion that remains in the atmosphere may be increasing.

NOAA ESRL launched the “Carbon Tracker” (information online at www.ersl.noaa.gov/gmd/ccgg/carbontracker), a new tool that uses observations and a state-of-the-art model to keep track of time-dependent emissions and the uptake of atmospheric CO_2 from both natural and anthropogenic processes. For the period from January 2001 to December 2006, Carbon Tracker estimated that the uptake of carbon by North American ecosystems averaged $-0.65 \pm 0.75 \text{ Pg C yr}^{-1}$; this can be compared to the total North American fossil fuel emissions of 1.9 Pg C yr^{-1} .

2) METHANE—E. J. Dlugokencky and R. C. Schnell

The CH_4 contribution to anthropogenic radiative forcing, including direct and indirect effects, is about 0.7 W m^{-2} (about half that of CO_2). Changes in the burden of CH_4 feed back into atmospheric chemistry, affecting the concentrations of OH and O_3 . The increase in CH_4 since the preindustrial era is responsible for $\sim 1/2$ of the estimated increase in background tropospheric O_3 during that time. Changes in OH concentration affect the lifetimes of other greenhouse gases, such as the replacement refrigerants (HCFCs and HFCs).

High-precision measurements of atmospheric CH_4 provide climate modelers with current and past rates of CH_4 increase, and they are also useful in constraining the global CH_4 budget and how it is changing with time. This “top-down” approach can determine total global emissions to within $\pm 10\%$, but background atmospheric observations alone cannot effectively quantify emissions from individual sources. A recent surprise in the global CH_4 budget was the report that vegetation can be a significant source of atmospheric CH_4 , even under aerobic conditions (Keppler et al. 2006). Our inability to identify this source before now shows the limitations of observations, particularly in the Tropics, for quantifying weakly emitting, diffuse sources.

In Fig. 2.15b, CH_4 mole fractions from the NOAA observatory at Mauna Loa, Hawaii, are plotted as a

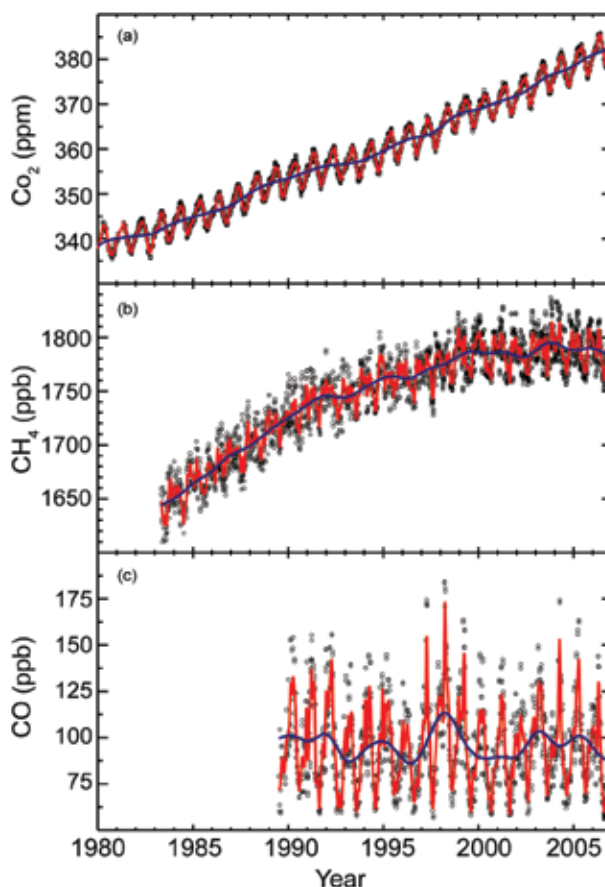


FIG. 2.15. Trace gas mole fractions (black symbols) determined from samples collected at the NOAA/ESRL Mauna Loa Observatory (MLO) for (a) CO_2 (T. J. Conway, NOAA), (b) CH_4 (E. J. Dlugokencky, NOAA), and (c) CO (P. C. Novelli, NOAA). In all panels, the solid blue line is the deseasonalized trend and the red line is a smooth curve fitted to the black symbols. Current trends at MLO are available online (www.cmdl.noaa.gov/ccgg/trends/; additional plots can be found at www.cmdl.noaa.gov/ccgg/).

function of time. During more than 20 years of measurements CH_4 has increased by nearly 10%, but the rate of increase has slowed in recent years. A large increase in 1998 and a smaller one in 2003 were likely the result of climatic conditions that resulted in increased emissions from biomass burning and natural wetlands. Otherwise, atmospheric CH_4 has remained nearly constant (Dlugokencky et al. 2003). Possible causes for the recent lack of growth in atmospheric CH_4 burden are decreased emissions from natural wetlands because of widespread drought in the Tropics (Bousquet et al. 2006), and a change in the CH_4 sink because of increased lightning (Fiore et al. 2006); but, the exact causes are still unclear. Our preliminary global annual CH_4 average for 2006 of 1775.4 ppb is only 3 ppb greater than that observed in 1999.

3) CARBON MONOXIDE—E. J. Dlugokencky and R. C. Schnell

Unlike CO_2 and CH_4 , CO does not strongly absorb terrestrial infrared IR radiation, but it still impacts climate through its chemistry. The chemistry of CO affects OH (which influences the lifetimes of CH_4 and HFCs) and tropospheric O_3 (itself a greenhouse gas), so emissions of CO can be considered equivalent to emissions of CH_4 (Prather 1996). Current emissions of CO may contribute more to radiative forcing over decadal time scales than emissions of anthropogenic N_2O (Daniel and Solomon 1998).

The CO mole fractions from Mauna Loa are plotted as a function of time in Fig. 2.15c and show little trend over the period of these measurements (Novelli et al. 2003). Superimposed on the flat trend are significant increases during 1997/98, and again in 2002/03, which were likely the result of tropical (Langenfelds et al. 2002) and boreal biomass burning (Kaschke et al. 2000). Because the lifetime of CO is relatively short (a few months), the anomaly quickly disappeared and CO returned to pre-1997 levels shortly afterward. In 2005, CO levels are comparable to those found in the early 2000s.

The preliminary globally averaged CO mole fraction in 2006 was 82.1 ppb, which is 1.1 ppb less than the 2005 global annual mean and 13.5 ppb lower than 1998, which had a large contribution from CO emitted by biomass burning.

4) DECREASES IN OZONE-DEPLETING GASES AND THEIR REPLACEMENTS—S. A. Montzka and R. C. Schnell

Long-lived halocarbons affect the radiative balance of the atmosphere because they efficiently absorb terrestrial IR radiation. Halocarbons containing Br and Cl also influence the radiative atmospheric bal-

ance indirectly through their destruction of stratospheric O_3 (see section 5c).

Because of concerns over stratospheric O_3 depletion, the production of many halocarbons has been restricted in recent years. The international phase-out of human-produced halocarbons was brought about through amendments and revisions to the 1987 Montreal Protocol on Substances that Deplete the Ozone Layer. As a result of these efforts, mixing ratios of many ozone-depleting gases have been declining at the Earth's surface in recent years; this decline continued in 2006 (Fig. 2.16). It is now apparent from the NOAA/ESRL/GMD measurements from around the globe that tropospheric mixing ratios of CFC-12, the longest lived and most abundant human-made ozone-depleting gas in the atmosphere, peaked within the last few years and now has begun to decrease.

The NOAA/ESRL/GMD data show that mixing ratios of some halogenated gases continue to increase globally (Fig. 2.16). The most rapid increases are observed for HCFCs and HFCs, which are chemicals commonly used as replacements for CFCs, halons, and other ozone-depleting gases. Although HCFCs contain Cl and deplete O_3 with a reduced efficiency compared to that of CFCs, HFCs do not participate in ozone-destroying reactions.

Increases in HCFCs have slowed notably in recent years; by mid-2006, the Cl in the three most abundant HCFCs amounted to 227 ppt, or 8.4 % of all Cl carried by long-lived halocarbons. Mixing ratios of HFC-134a (1, 1, 1, 2-tetrafluoroethane), the most abundant HFC in the global background atmosphere, increased nonlinearly in the 1990s during the period of early production and use. From 2001 to 2006, however, it has increased in the global troposphere at a fairly constant linear rate of 4.3 ppt yr^{-1} . Concern over increases in HFCs stems in large part from the fact that these gases are efficient absorbers of infrared radiation.

The influence of these disparate trends on future levels of stratospheric O_3 can be gauged roughly from a sum of Cl and Br in long-lived halocarbons, provided the enhanced efficiency for Br to destroy O_3 is considered [note that this efficiency factor has been updated here to 60 based upon a reanalysis appearing in the latest WMO Scientific Assessment of Ozone Depletion (Cunnold et al. 2007)]. This sum is expressed here as EECl (Fig. 2.16), and is derived from surface-based measurements. EECl provides an estimate of the ozone-depleting power of trace gases a few years in the future, when air at the Earth's surface will have become mixed into the midlatitude stratosphere where the O_3 layer resides. A second metric,

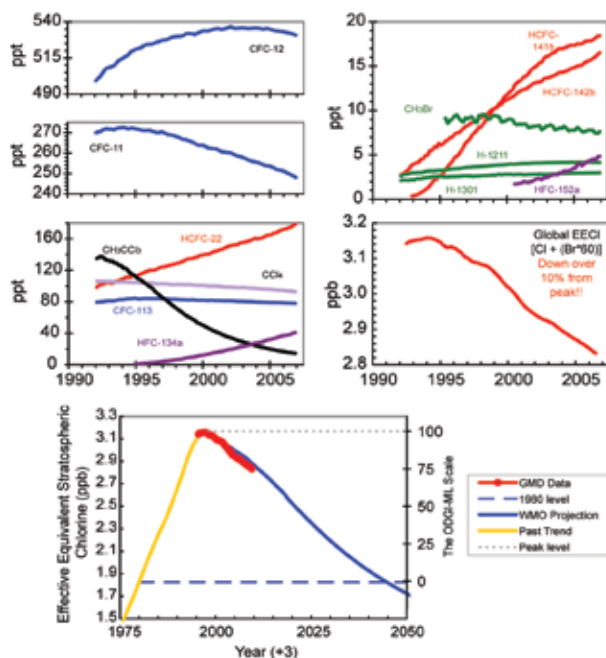


FIG. 2.16. Changes in global mean tropospheric mixing ratios (ppt, or pmol mol^{-1}) of the most abundant CFCs, HCFCs, HFCs, chlorinated solvents, and brominated gases. These global changes are calculated from atmospheric measurements made at remote sites in both the Northern and Southern Hemisphere (from the NOAA/ESRL/GMD cooperative air sampling network). The middle-right hand panel shows secular changes in atmospheric EECl (in ppb or nmol mol^{-1}), which is an estimate of the ozone-depleting power of atmospheric halocarbons. EECl is derived from observed mixing ratios of ozone depleting gases appearing in the other 4 panels, and it is derived from the sum of $[\text{Cl} + (\text{Br} \times 60)]$ contained in these gases. The bottom panel shows the recent changes in EESC observed by the NOAA/GMD global network relative to the secular changes observed in the past, including the level observed in 1980 when the ozone hole was first observed, and a projected future. The Ozone Depleting Gas Index for midlatitudes is derived (right-hand axis) from rescaling EESC. EESC is derived from EECl by simply adding 3 yr to the time axis to represent the lag associated with mixing air from the troposphere to the middle stratosphere, where the ozone layer resides. [Source: S. A. Montzka, J. H. Butler, G. Dutton, D. Mondeel, and J. W. Elkins, NOAA/GMD.]

EECl provides an estimate of the ozone-depleting power of trace gases in the near future for the stratosphere over the polar regions (not shown).

The observations indicate that the EECl and ECl content of the lower atmosphere has declined fairly steadily since the peak in 1994 to 2006 at a mean rate of $27\text{--}29 \text{ ppt yr}^{-1}$. Scenarios projecting future halo-

carbon mixing ratios have been derived elsewhere based upon full compliance with the fully amended and revised Montreal Protocol and our understanding of the atmospheric lifetimes of these gases (Cunnold et al. 2007). These analyses suggest that it will take 40–60 years for EECl and ECl to decline to the levels present in 1980, which is before O_3 depletion was first observed. This 1980 level is notable, given that one might expect nearly full recovery of stratospheric O_3 once atmospheric EECl or ECl returns back to this level. The time scale for O_3 recovery will depend upon other factors as well, however, such as stratospheric temperatures and atmospheric aerosol loading. Nonetheless, the declines in EECl from 1994 to the present represent a significant drop in the atmospheric EECl burden; as of 2006 EECl had declined 20% of the way back down to the 1980 level (lower panel of Fig. 2.16).

Progress toward EECl returning to the abundance in 1980 can now be readily assessed with the NOAA ODGI (online at www.cmdl.noaa.gov/odgi/). This index is derived from EECl and ECl data for the midlatitude and Antarctic stratosphere. The index is scaled so that a value of 100 represents the EECl or ECl abundance at its peak, and 0 represents the 1980 level (the level at which no ozone depletion is expected, assuming constancy in all other variables). In 2005, the ODGI-Midlatitudes was 76.7, indicating that the abundance of ozone-depleting substances have decreased nearly 25% of the way toward the levels that were present in 1980 (Fig. 2.16). Less progress is evident for Antarctica; ODGI-Antarctica was 87.6 in 2005, which suggests halocarbon abundances have declined slightly over 12% of the way down to 1980 levels.

Changes in the direct radiative influence of long-lived halocarbons can be estimated from observed changes in atmospheric mixing ratios with knowledge of trace-gas radiative efficiencies. Such an analysis suggests that the direct radiative forcing of these gases was still increasing in 2005, though at a much slower rate than observed from 1970 through 1990.

5) THE COMBINED INFLUENCE OF LONG-LIVED TRACE GASES ON THE RADIATIVE BALANCE OF THE ATMOSPHERE—S. A. Montzka and R. C. Schnell

Changes in the abundance of long-lived trace gases have a direct and indirect influence on the energy balance of the atmosphere. The direct radiative influence of a trace gas is directly proportional to its atmospheric abundance and how efficiently it absorbs infrared radiation in specific regions of the electromagnetic radiation spectrum (its radiative

forcing). High-precision measurements of CO₂, CH₄, N₂O, CFC-12, and CFC-11 (the major greenhouse gases), along with 10 minor greenhouse gases obtained from the NOAA global air sampling network, have been used to calculate the overall change in the direct radiative climate forcing arising from the sum of all of these long-lived gases (Hofmann et al. 2006) (Fig. 2.17). This forcing is calculated by considering changes in the abundances of these gases since 1750. By mid-2005, the increases in the abundances of all of these gases above 1750 levels amounted to an additional radiative forcing to the atmosphere totaling approximately 2.6 W m⁻². Changes in the abundance of CO₂ since 1750 accounted for nearly two-thirds of this enhanced radiative heating.

The NOAA AGGI has been developed based upon the radiative forcing calculated from these NOAA measurements (Hofmann et al. 2006). The index is a ratio of radiative forcing from all of these gases (based upon changes since 1750) relative to the radiative forcing calculated from these gases for 1990, the Kyoto Protocol baseline year. By 2005, the AGGI was 1.215, indicating that the direct radiative forcing arising from increases in the abundance of these trace gases had increased by 21.5% from 1990 to 2005 (Fig. 2.17). Increases in the atmospheric abundance of CO₂ accounted for over 75% of the observed increase in the AGGI from 1990 to 2005.

6) NITROUS OXIDE AND SULFUR HEXAFLUORIDE—J. W. Elkins and G. S. Dutton

Nitrous oxide and SF₆ are strong infrared-absorbing greenhouse gases and are measured on the same gas chromatographic instrument channel at all of NOAA's Earth System Research Laboratory baseline observatories. Molecules of N₂O and SF₆ in the atmosphere are 296 and 22,200 times more effective infrared absorbers per molecule compared to CO₂ over a 100-year time horizon, respectively. However, the concentrations of N₂O and SF₆ are just over 1000 and 60 million times lower than the atmospheric CO₂ concentration, respectively. At the end of 2006, the mean atmospheric concentrations of N₂O and SF₆ were 320 ppb and 6 ppt, respectively, as shown in Fig. 2.18. The current climate forcing relative to the beginning of the industrial revolution (1750) for N₂O and SF₆ is 0.16 and 0.002 W m⁻², respectively. While the climate forcing from SF₆ is small, it has a longer lifetime (500–3500 yr) than N₂O (100 yr). Atmospheric N₂O also affects stratospheric O₃ because it is the source gas for stratospheric NO. Stratospheric NO contributes to the NO_x catalytic sink for stratospheric O₃ loss, which is dominant between 25 and 40 km.

Another striking feature of these greenhouse gases is their almost linear growth rate over their full atmospheric records (Fig. 2.18). Atmospheric N₂O and SF₆ are growing at 0.77 ppb yr⁻¹ and 0.22 ppt yr⁻¹, respectively. Atmospheric N₂O has both natural and manmade sources, where the manmade sources (fertilizer usage, catalytic reduction of fossil fuel emissions, by-products of chemical processes, etc.) account for about 30% of total emissions. Whereas SF₆ is produced solely by man, its usage is now considered essential as an insulator for the distribution of electric power (95%) with minor usage in atmospheric tracer studies. There are biennial and short-term changes in the atmospheric growth rates of N₂O and SF₆ that are greater than ±25%. These changes are related to varying source strengths on the ground, in transport, and as destruction in the upper atmosphere. The decline in the growth rate of SF₆ after 1996 is most likely the result of voluntary recovery of SF₆ by utility companies and elimination of the use of SF₆ as a compressed gas in automobile tires, and the switch to the use of other gases or materials for bladders in the soles of athletic shoes.

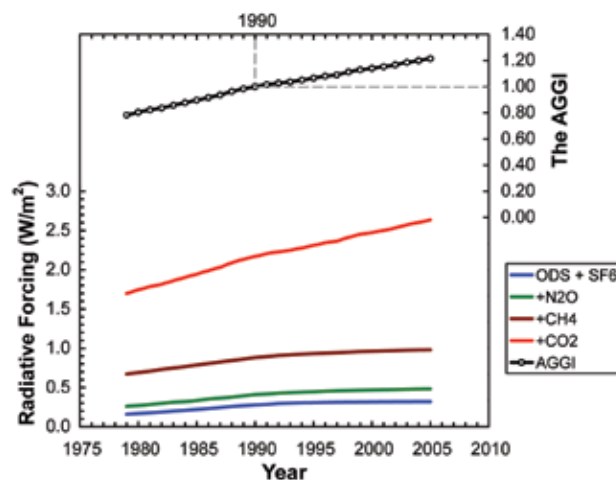


FIG. 2.17. The direct radiative forcing arising from increases in the abundance of long-lived trace gases in the atmosphere since 1750 and the Annual Greenhouse Gas Index (Hofmann et al. 2006). The colored lines indicate the radiative forcing from different subsets of gases including ozone-depleting substances and SF₆ (indicated as “ODS+SF₆”), the additional contribution of N₂O (indicated as “+N₂O”), the additional contribution of CH₄ (indicated as “+CH₄”), and the additional contribution of CO₂ (indicated as “+CO₂”). The total direct radiative forcing from all these gases is equivalent to the line indicated as “+CO₂.” Also shown is the NOAA AGGI, which is calculated from the total direct radiative forcing normalized to 1990, the baseline year of the Kyoto Protocol.

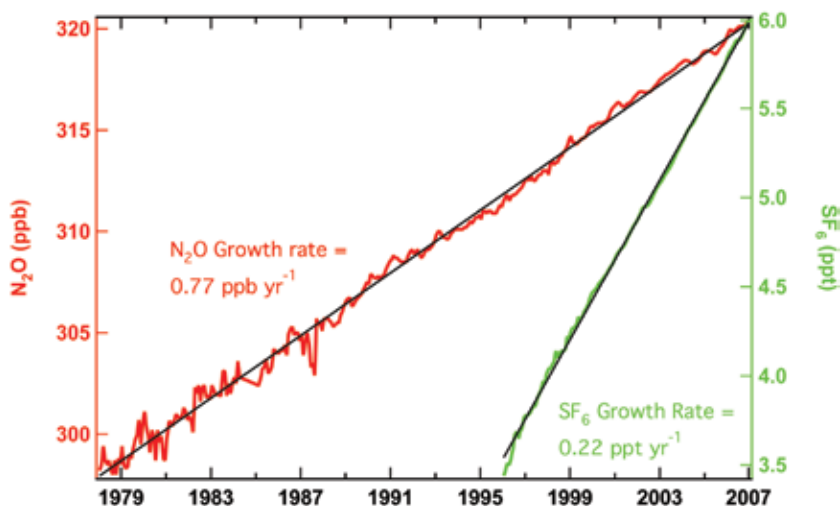


FIG. 2.18. The global atmospheric concentration of N_2O versus time from flasks (1977–87) and in situ gas chromatographs (1988–2006) at NOAA/Earth System Research Laboratory baseline stations at Pt. Barrow, Alaska; Niwot Ridge, Colorado; Mauna Loa, Hawaii; American Samoa; and South Pole is shown in red. The global trend for atmospheric SF_6 from flasks (1996–99) and in situ gas chromatographs (2000–06) is shown in green. Calculated linear regression lines are shown in black. [Source: J. W. Elkins and G. S. Dutton, NOAA/ESRL.]

7) AEROSOLS—A. T. Evan, N. M. Mahowald, and L. A. Remer

The global aerosol system in 2006 was both typical and atypical of long-standing patterns. Figure 2.19 shows the annual mean AOD at 550 nm, calculated from daily MODIS 10-km retrievals (Remer et al. 2005). The AOD is a measure of the extinction of shortwave radiation, and its global distribution is roughly equally divided between dust, sulfates, and carbonaceous aerosols, even though dust and sea salt dominate the aerosol mass loading. This is because sulfates and carbonaceous species are much more efficient in terms of light extinction (Tegen et al. 1997). Note that the standard MODIS algorithm does not retrieve either over clouds, or over snow, ice, sunglint, or bright desert surfaces. Thus, the aerosol distribution of Fig. 2.19 is biased toward summer retrievals in high-latitude and cloud-free high pressure systems.

For long time series analysis, we use data from longer-flying satellites, for example, the AVHRR, since the MODIS data record begins in 2000. Here we use the 870-nm AOD (Ignatov and Stowe 2002a,b) and dust fraction (Evan et al. 2006) products from the Pathfinder Atmospheres Extended dataset (online at <http://cimss.ssec.wisc.edu/clavr/patmosx.html>). This dataset applies a new calibration technique to the AVHRR imagers (Heidinger et al. 2002), making it more apt for studying long-term changes. However, aerosol activity over land and in the presence of

clouds is not detectable and therefore must be inferred either by over-water clear-sky retrievals or by comparison with MODIS retrievals. We also include output from a reanalysis-driven transport model that includes mineral aerosol source and deposition algorithms (Mahowald et al. 2003).

(i) Saharan and Sahelian output

While some of the aerosols produced from this region include carbonaceous aerosol from biomaburning, biofuels, and urban sources, mineral dust provides the bulk of the mass exported over the Atlantic Ocean. Mineral aerosols from west and central Africa have been shown to account for ~50% of the global dust loading (Luo

et al. 2004) and, therefore, are responsible for ~20% of the global aerosol optical thickness (Tegen et al. 1997). Figure 2.20 is a plot of the changes in annual mean dust concentration observed in Barbados (Prospero et al. 2003) and seen by the AVHRR for the western North Atlantic (0° – 30°N , 10° – 60°W). According to the AVHRR dust product, loadings over the western North Atlantic were below the climatological mean for 2006 (this was also found to be true over the Mediterranean). However, this low level of activity is not statistically significant and reflects a

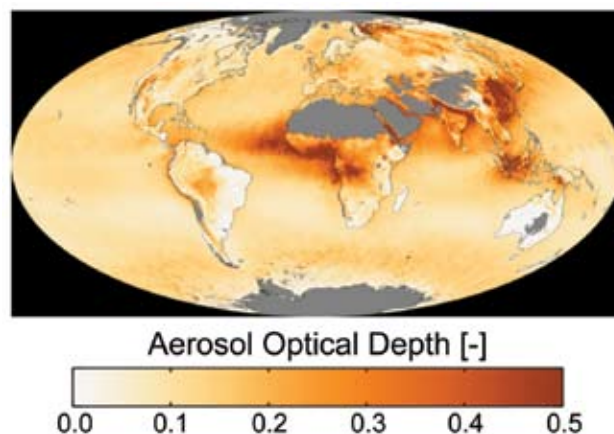


FIG. 2.19. Map of global mean AOD values at 550 nm from the MODIS for 2006. Regions in gray denote missing values.

downward trend in the data over the last 20 years. Additionally, a strong downward trend in dust is not seen in the Barbados data, which show an increase in dustiness from the mid-1960s through the early 1980s, and then a leveling off of dustiness. This disagreement may simply result from comparing dust-frequency satellite data of model output averaged over a large area, with concentration amounts from a point source. Model output also corroborates a decline in dust activity for 2006, with amounts for January–October below the climatological mean (1979–2005). The 2006 annual mean AOD for this region from MODIS is the lowest of all seven years in the MODIS record.

(ii) India

The Indo-Gangetic Plain in India consistently shows elevated AOD that is a combination of locally produced pollution from urban/industrial aerosol, biofuel, and biomass burning during the winter months, and transported desert dust from both the Arabian and Thar Deserts in the premonsoon and summer months. The MODIS AOD shows that 2006 was typical in terms of mean annual AOD, according to the seven years of available data.

(iii) China and the Yellow Sea

Eastern China and the surrounding Yellow Sea contained some of the heaviest aerosol loading in 2006, and is one of the few areas in the AVHRR data to show a statistically significant departure (increase)

from the mean state in 2006. It is probable that dust from the upwind deserts (whose activity peaks during boreal spring) and urban/industrial aerosols from nearby population centers contribute to these higher-than-normal aerosol concentrations. The MODIS data show a strong increase in fine-mode aerosol amounts in the summer of 2006, as well as an increase in coarse-mode aerosol during April and May. This suggests that the elevated aerosol amounts may result from increases in dust aerosol during the spring and urban/industrial aerosol or transported biomass burning smoke during the summer. However, the increases in 2006 are corroborated neither by the model output, which shows near-normal activity for 2006 in this region, nor by observations made at Midway Island (Prospero et al. 2003).

(iv) Indonesia

Aerosol optical thickness maps of the areas surrounding Indonesia show above-average aerosol loadings for the boreal summer and fall that are statistically significant. These elevated levels of aerosols are likely the result of smoke from biomass burning. October 2006 has the highest single monthly mean value of AOD in the entire 7-yr MODIS record for this region. It is probable that the positive-phase ENSO event and the accompanying decrease in precipitation are key factors in this increase of aerosol loadings (van der Werf et al. 2004). An analysis of aerosol values for the bodies of water surrounding the Indonesian islands reveal a similar (but much greater) response during the ENSO event of 1997.

(v) Eastern Europe, the boreal forests, and the Arctic

The MODIS AOD dataset shows high aerosol loading over eastern Europe, Siberia, and the adjoining Arctic Ocean. These aerosols were produced by the biomass burning of agricultural lands and boreal forests in Russia during May, transported across Scandinavia and into the Arctic (Stohl et al. 2006). The MODIS picture is slightly misleading. Because of snow and ice cover, MODIS retrievals are possible only in a limited part of the year. An aerosol event that occurs in the short summer season will be exaggerated in the annual mean values calculated from the MODIS retrievals. The 2006 Siberian smoke season is the second strongest in the 7-yr MODIS record, exceeded only by the 2003 season. In contrast, boreal forest smoke that was prevalent in North America in 2002 (Quebec, Canada) and 2004 (Alaska) is mostly absent in 2006. Interannual boreal fires and the aerosols they produce are almost entirely depen-

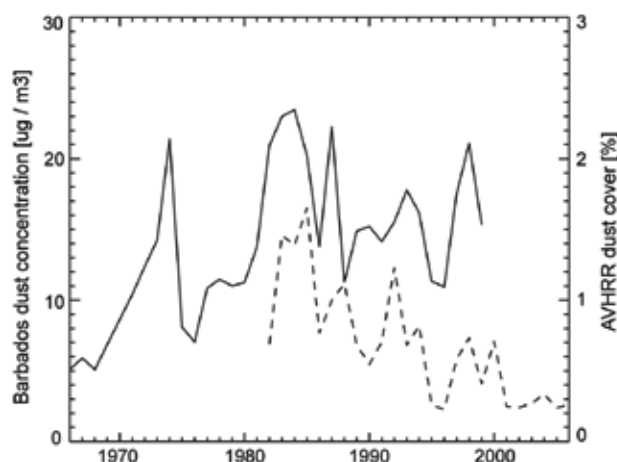


FIG. 2.20. Annual mean time series of soil dust over the North Atlantic. The solid line represents annual mean dust concentrations observed in Barbados for the years of 1966–99. The dashed line is the annual mean dust cover as seen by the AVHRR imager over the western North Atlantic (0°–30°N, 10°–60°W) for the years of 1982–2006.

dent on natural causes that include precipitation and humidity patterns, soil moisture left from winter snow cover, and lightning strikes. However, forest management practices also play a part.

(vi) Amazon basin

One of the more interesting aerosol stories of 2006 was the sudden decrease of biomass-burning aerosol in the Amazon basin, noted in Fig. 2.19 by annual mean AOD values of less than 0.25. The drought in 2005 created one of the heaviest smoke seasons on record in the Amazon. In 2006, continued drought in the beginning of the season threatened a repeat of the previous year. A combination of enforced fire regulations changed cultural practices, and an early onset of the rain in the latter part of the season cut the seasonal mean AOD values to roughly half of what they had been in 2005 (Koren et al. 2007, manuscript submitted to *Environ. Res. Lett.*).

e. *Global winds*—M. A. Bourassa, R. N. Maue, S. R. Smith, P. J. Hughes, and J. Rolph

1) OCEAN SURFACE WINDS

Wind speeds for ice-free regions for the period from July 1999 to 2006 are obtained using the SeaWinds scatterometer on the QuikSCAT satellite. Technically, this instrument also responds to changes in the air-sea temperature difference; however, variability resulting from temperature is usually relatively small compared to changes in wind speed. Monthly averaged speeds are determined for January 2000 through December 2006. The range of anomalies in 2006 is large, similar to that of 2003 and 2004, and much greater than that of 2000, 2001, and 2005. The month-to-month changes in 2006 are also relatively large. Note that an increase in wind speeds is typically associated with a greater rate of transfer of energy from the ocean to the atmosphere. For low-wind speeds regions, such a change would result in only an $\sim 1 \text{ W m}^{-2}$ change in the rate of heat transfer. For high-wind speeds regions, the

change could exceed 5 W m^{-2} , which integrated over a month is a very large extra input of energy to the atmosphere.

(i) Tropics

Some regional changes (Fig. 2.21) in wind speeds are steadier than suggested in the global average. The El Niño-related atypical position of the SPCZ is evident in the last half of the year. Similarly, from June onward there are greater wind speeds in the western Pacific Ocean warm pool and increased westward winds in the eastern central Pacific Ocean. There are also changes in the subtropical North Atlantic related to an eastward displacement of the Bermuda high, which could have contributed to the reduction in the number of landfalling tropical cyclones. Increased wind speeds in the western subtropical Atlantic Ocean in September and October are indicative of greater vertical wind shear, which would also tend to inhibit the strengthening of tropical cyclones.

(ii) Northern oceans

Monthly anomalies in the NH show westerlies that are stronger than usual for most of the year and pos-

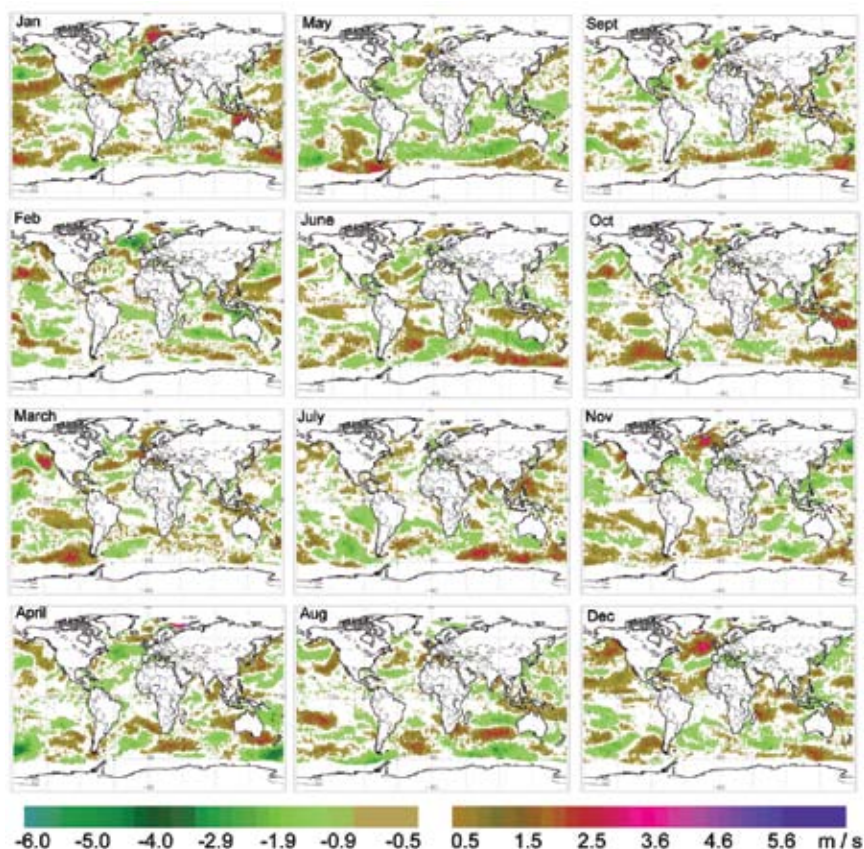


FIG. 2.21. Regional wind speed anomalies for January–December 2006.

sibly shifted farther north than usual. Wind anomalies in the Gulf of Alaska are indicative of stronger westerly-to-southwesterly flow that lasted from May into October. Late in the year, the North Atlantic was dominated by a strong Icelandic low (November and December). This resulted in stronger winds throughout the ocean between Greenland and Europe. An anomalous ridge near the eastern seaboard of the United States during the same months is apparent in negative wind anomalies and the resulting warm start to the 2006/07 winter.

(iii) Southern Ocean

There are also long periods of increased wind in the Southern Ocean. The most notable location is

south of Australia (May–July, September–December). Examination of daily wind fields shows that some of these greater wind speeds are associated with offshore flow from the eastern Antarctic ice dome. They may be an indicator of stronger katabatic wind flow from the interior of Antarctica. These katabatic flows may not be directly responsible for the higher over-ocean winds, but they have been shown to increase convergence and cyclogenesis in the circumpolar trough. The result would be an increase in wind speeds.

2) LAND SURFACE WINDS

Monthly wind speed anomalies (Fig. 2.22) with respect to the long-term mean (1968–96) were calculated from data obtained from the NCEP–NCAR

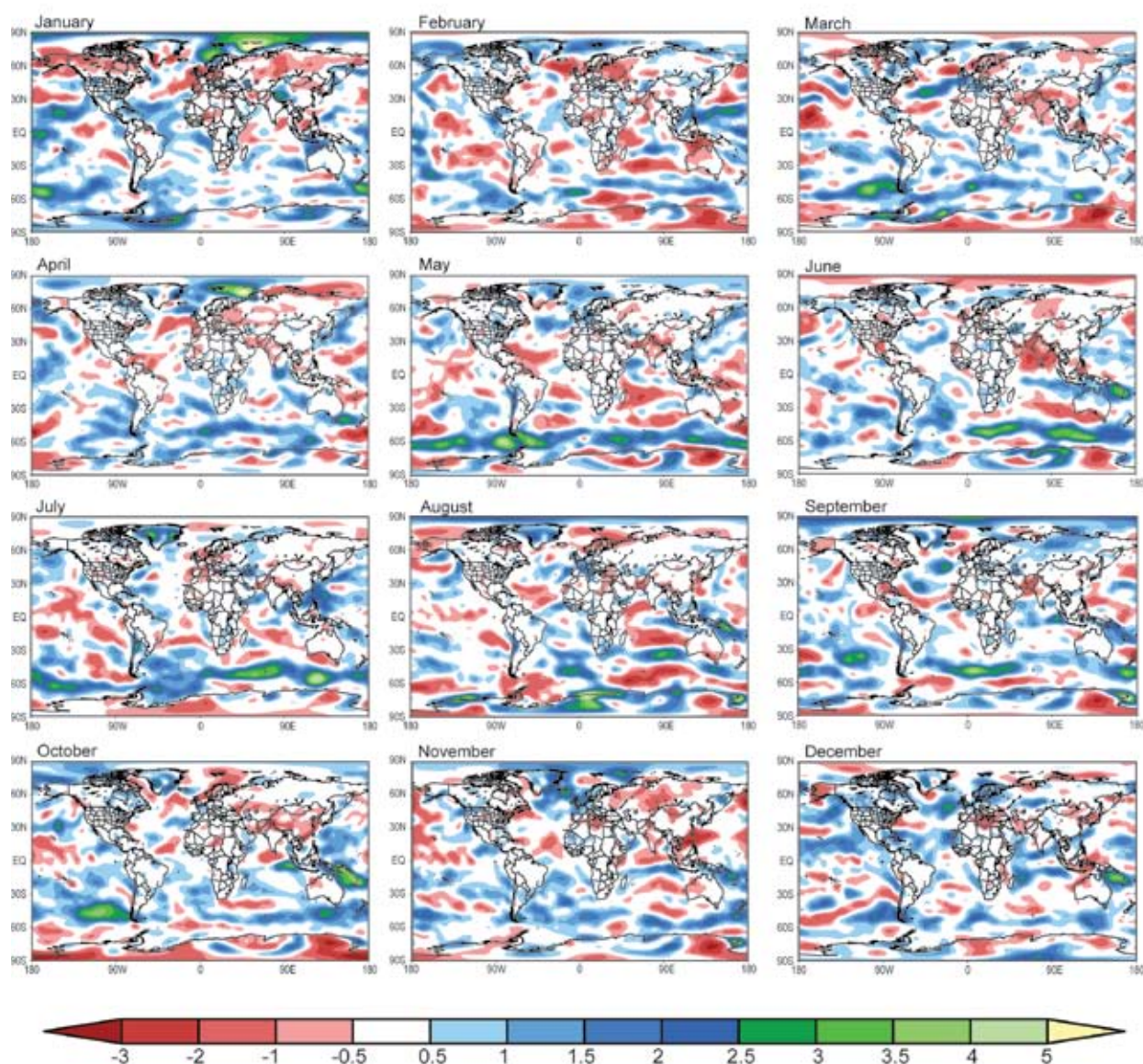


FIG. 2.22. Global monthly mean wind speed anomalies obtained from NCEP–NCAR reanalysis for January–December 2006 (m s^{-1}).

reanalysis (Kalnay et al. 1996). The oceanic wind speed anomalies are qualitatively similar to the QuikSCAT-derived wind speeds over the oceans and ice edges especially in the polar regions. Differences in spatial resolution between the two datasets (QuikSCAT: $\sim 0.25^\circ$ versus NCEP–NCAR: $\sim 2.5^\circ$) explain the difference in magnitudes. It is important to note that QuikSCAT winds are not assimilated into the reanalysis product.

The wind speed anomaly patterns over most of the world's landmasses are small or inconsistent from month to month, with relatively small magnitudes compared with the adjacent ocean. Stronger-than-normal wind speeds persisted over the Arctic, including Greenland, Alaska, and Siberia throughout winter. For the remainder of the year, Greenland experienced above-average winds. Notable small-magnitude negative wind speed patterns persisted over the Indian subcontinent during spring and early summer. In the Southern Hemisphere, there is evidence of considerable wind speed anomalies of both signs over Antarctica, possibly a result of varying cyclolysis regions and katabatic wind regimes. The austral spring over the tip of South America also experienced stronger-than-normal wind speeds.

f. Teleconnection patterns and blocking—W. Higgins and M. L'Heureux

Teleconnection patterns are recurrent and persistent large-scale patterns of pressure and circulation anomalies that span large geographical areas. They reflect large-scale changes in the atmospheric wave and jet stream patterns, and influence temperature, rainfall, storm tracks, and jet stream location and intensity over vast distances. Thus, they are often responsible for abnormal weather patterns occurring simultaneously over regions separated by great distances. Although these patterns typically last from several weeks to several months, they can sometimes be prominent for consecutive years or longer, reflecting an important part of both the interannual and interdecadal variability of the atmospheric circulation. The focus of this section is on the NAO, PNA, and WP teleconnection patterns. Monthly index values for the NAO, PNA, and WP teleconnection patterns over the last few years are shown in Fig. 2.23. The NOAA/CPC provides daily and monthly time series for other NH teleconnection patterns and details about the analysis procedure used to obtain them (information online at www.cpc.ncep.noaa.gov/data/teledoc/telecontents.shtml).

Atmospheric blocking is characterized by an interruption or splitting of the normal westerly flow

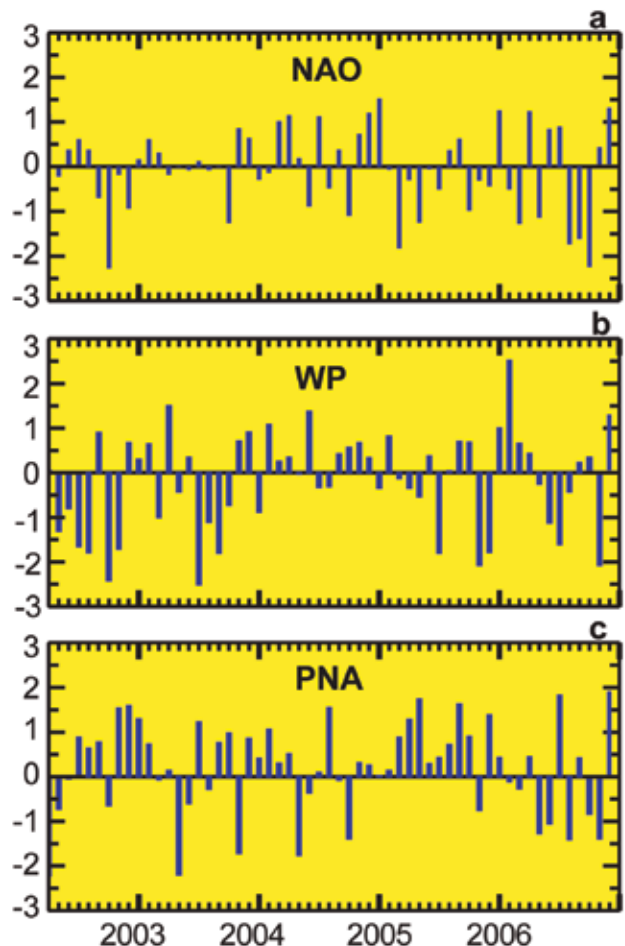


FIG. 2.23. Standardized time series of the monthly (a) NAO, (b) WP, and (c) PNA teleconnection indices for the period 2003–06. The teleconnection patterns are calculated from a RPCA applied to monthly standardized 500-hPa height anomalies during 1950–2000. The anomalies are standardized by the base period monthly means and standard deviations. Additional discussion on how the teleconnection indices are calculated is found online at www.cpc.ncep.noaa.gov/data/teledoc/telecontents.shtml. [Source: CPC.]

around a ridge of high pressure into two separate branches over a considerable longitudinal extent. Common characteristics include easterly flow to the south of the blocking ridge and pronounced meridional flow both upstream and downstream of the blocking ridge. As a consequence, the normal eastward progression of synoptic disturbances is obstructed, leading to episodes of prolonged extreme weather conditions. On intraseasonal time scales the persistent weather extremes can last from several days up to a few weeks, often accompanied by significant temperature and precipitation anomalies. Preferred areas for atmospheric blocking, especially during the NH cold season, include the North Pacific and north-

eastern Atlantic.

NOAA/CPC routinely monitors atmospheric blocking and is involved in continuing research to better understand its role in the global climate system. The procedure used to identify blocking is based on the blocking index of Tibaldi and Molteni (1990), modified from that of Lejenas and Okland (1983). The index calculation, together with current conditions, blocking outlooks, and blocking composites, is readily available from the CPC Web site (www.cpc.ncep.noaa.gov/products/precip/CWlink/MJO/block.shtml).

1) DESCRIPTION OF TELECONNECTION PATTERNS

The NAO is a metric of the meridional pressure gradient over the North Atlantic Ocean (see Hurrell 1995; Barnston and Livezey 1987), and is highly correlated with the AO (e.g., Wallace 2000; Thompson and Wallace 1998). The most conspicuous attribute of the PNA is a “wave train” of action centers that stretch from the subtropical North Pacific to Florida, with intermediate action centers near the Aleutians and in central Canada (see Wallace and Gutzler 1981). ENSO is related to a PNA-like pattern in the extratropics. El Niño (La Niña) tends to be associated with the positive (negative) phase of the PNA pattern.

The West Pacific pattern consists of a north–south dipole of anomalies, with one center located over the Kamchatka Peninsula and another broad center of the opposite sign covering portions of southeastern Asia and the western subtropical North Pacific. A third anomaly center is located over the eastern North Pacific and southwestern United States. Strong positive or negative phases of this pattern reflect pronounced zonal and meridional variations in the location and intensity of the entrance region of the Pacific jet stream. The positive phase is associated with above-average precipitation in all seasons over the high latitudes of the North Pacific, and below-average precipitation extending across the central North Pacific toward the west coast of North America; the opposite is true for the negative phase.

2) RECENT MONTHLY TELECONNECTION INDEX VALUES

For 2006 as a whole, both the NAO and PNA were dominated by the negative phase, though there were notable monthly excursions into the positive phase (e.g., the PNA during July 2006). The WP pattern was generally positive during early 2006, with strong negative excursions during NH summer and during November 2006. During February 2006, the 500-hPa circulation pattern in the extratropics featured a pronounced north–south dipole of height anomalies

across the western and central North Pacific, which reflected a strong positive phase (+2.5) of the WP teleconnection pattern (Fig. 2.23b). The 500-hPa circulation pattern during August–October 2006 featured positive height anomalies over Greenland and the polar region, and negative height anomalies from the north-central United States to the United Kingdom; and over central Siberia. The eastern third of the United States tended to be colder than normal, especially in September and October, consistent with the strong negative values of the NAO index (Fig. 2.23a). During October, the NAO index value was –2.2, and for the August–October season, the NAO index value was –1.9. The October 2006 value (–2.2) was the most extreme since the October 2002 value (–2.3), when temperatures across the northern and eastern United States were also significantly below normal.

The NH 2005/06 winter was dominated by the negative phase of the NAO for the first time since 2000/01 (not shown). On the other hand, the PNA continued in its positive polarity for the fourth consecutive winter season (Fig. 2.24). Since 1995, the PNA has tended to be in the positive phase; 2006 was a bit of an exception in that the PNA index was negative during six calendar months.

3) DESCRIPTION OF BLOCKING EPISODES AND LINKS TO MAJOR CLIMATE ANOMALIES DURING 2006

Two examples that relate exceptional blocking

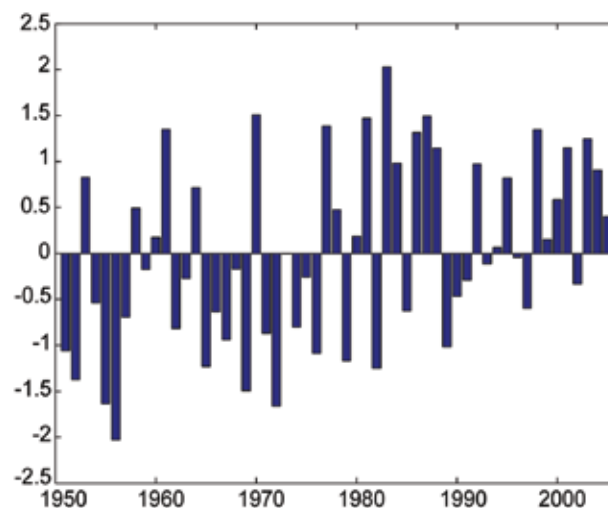


FIG. 2.24. Standardized time series of the PNA teleconnection indices for the period December–March 1950–2006. The labeling convention is such that 2005 indicates DJFM 2005/06. The procedure used to calculate the teleconnection patterns is briefly described in the caption to Fig. 2.23.

events to extreme weather conditions during 2006 are presented below. The latter event was associated with the negative polarity of the WP teleconnection pattern.

(i) *Excessive rainfall in New England during May 2006*

Record rainfall fell over portions of New England (specifically northeastern Massachusetts, southern New Hampshire, and southern Maine) during 12–15 May 2006, resulting in flooding in the region comparable to the most extreme events during the last 70 years. Rainfall totals at some locations exceeded 12 feet.

The blocking conditions developed in the beginning of May 2006 when a block formed in the vicinity of Scandinavia. As is quite often the case, the blocking ridge shifted westward with time (retrograde motion) at high latitudes, passing over Greenland (20°–50°W) during 6–12 May and over eastern Canada (60°W–90°) during 12–15 May (Fig. 2.25). The low-level (850 hPa) wind during 12–15 May (Fig. 2.26a) shows a cyclonic circulation covering the entire eastern United States. The persistent very strong southeasterly flow of moist

Atlantic air over central New England contributed greatly to the excessive rainfall totals observed in the region (Fig. 2.26b). Situations like this one often feature a “training” effect in which precipitating clouds move over the same area along the direction of the mean flow, resulting in excessive rainfall and flooding.

(ii) *Excessive rainfall in the Pacific Northwest during November 2006*

A strong upper-level ridge, which dominated the Gulf of Alaska and west coast of North America during October 2006, weakened late in the month. It was

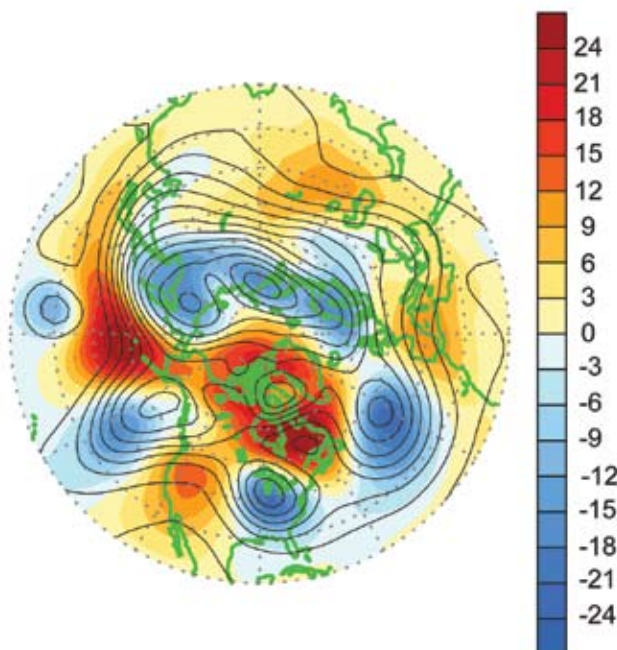


FIG. 2.25. Mean 500-hPa height (contours, contour interval 60 m) and height anomalies (shading, units are decameters) for 12–15 May 2006. Anomalies are departures from the 1979–95 base period means. The blocking ridge axis is indicated by the dotted white line, and the flanking trough axes are indicated by dashed white lines.

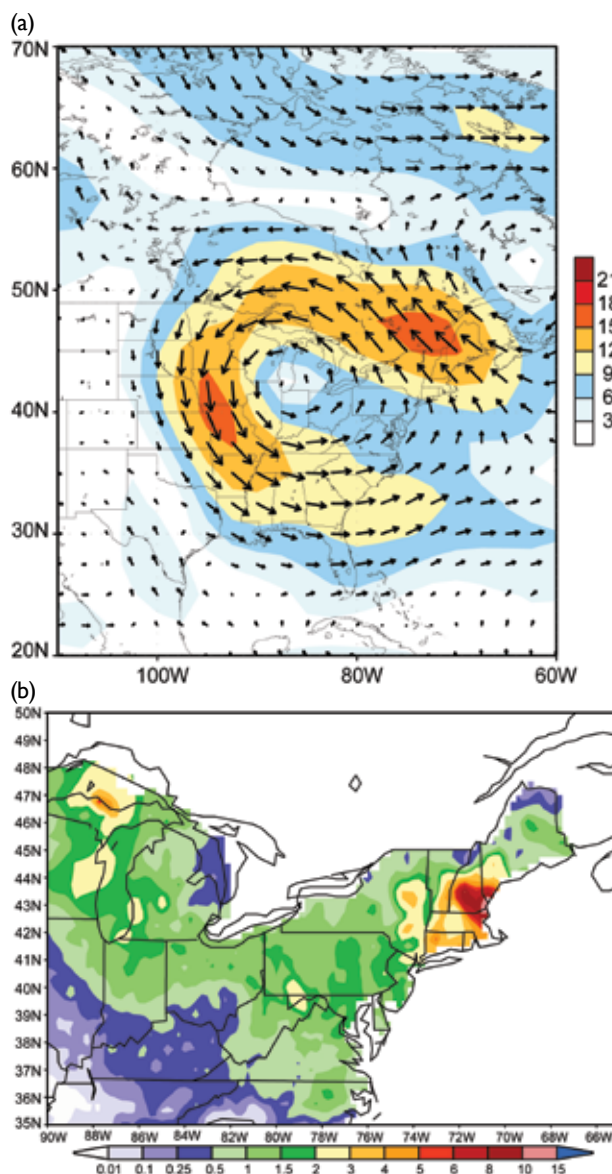


FIG. 2.26. (a) Mean 850-hPa wind vectors and wind speed (shading). Units: m s^{-1} . (b) Total precipitation (in.) for the period 12–15 May 2006.

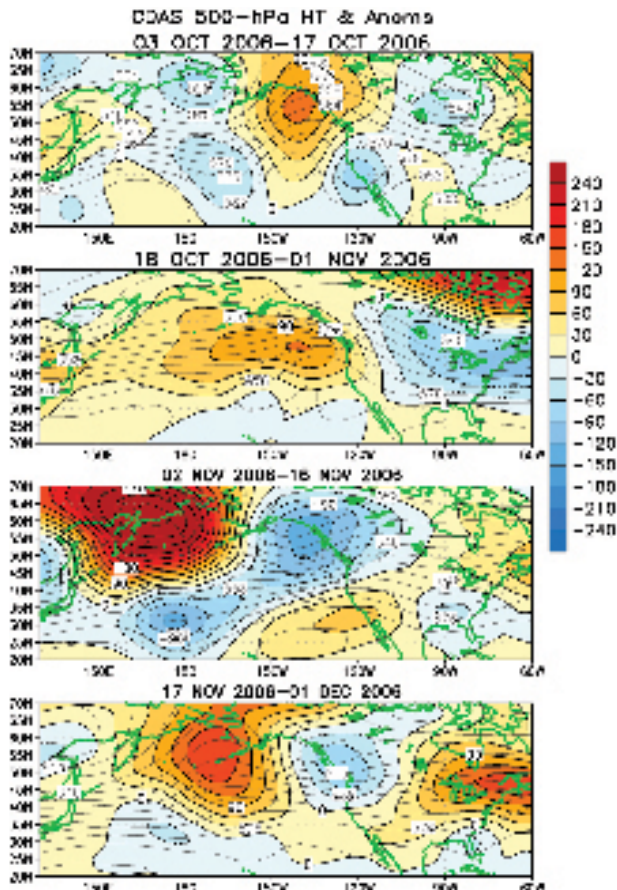


FIG. 2.27. 500-hPa heights (dm) and anomalies (m) over the North Pacific and North America during the 2-week periods indicated on each panel.

replaced by a persistent blocking pattern that developed over the high latitudes of the west-central North Pacific in early November (Fig. 2.27). The northern and southern branches of the Pacific jet stream recombined over the eastern North Pacific, contributing to a series of strong storms that resulted in remarkably wet and cold conditions in the Pacific Northwest, western Canada, and portions of Alaska during the first half of November 2006. This pattern projected very strongly on the negative phase of the WP teleconnection pattern during November 2006 (Fig. 2.23b).

It is important to note that the conditions during November 2006 were related to midlatitude variability, with little or no connection to the developing El Niño conditions in the tropical Pacific. In particular, these events occurred in advance of the development of El Niño–related enhanced convection near and to the east of the international date line, which typically leads to atmospheric coupling and an eastward shift of the subtropical ridges and the North Pacific jet stream during the NH winter.

3. GLOBAL OCEANS—J. M. Levy, Ed.

a. Overview—J. M. Levy

As the global ocean observing system matures, climatologies of essential climate variables are growing more robust, as are observations of anomalous departures that shed light on the evolving behavior of the coupled ocean–atmosphere system. Year 2006 exhibited numerous anomalies of interest:

- Global SST anomalies were primarily positive, notably so in boreal summer in the North Atlantic and in the latter part of the year in the central and eastern equatorial Pacific, associated with the 2006 El Niño.
- The mean of latent plus sensible heat flux was similar to that in 2005; total flux in both years was at the high end of a long-term upward trend that started in 1977/78. Significant heat flux anomalies were observed in the regions of the 2006 El Niño and Indian Ocean dipole mode event.
- Global sea surface salinity anomalies accentuated climatological patterns: freshwater regions were fresher and salty regions were saltier. The subpolar North Atlantic and Nordic Seas were anomalously salty in 2006.
- Dramatic westward surface current anomalies associated with the development of El Niño were observed late in the year in the tropical Pacific Ocean, while the seasonal reversal of currents was particularly pronounced on the equator in the Atlantic Ocean. Exchange of water between the South and North Atlantic Oceans was weaker than normal.
- The MOC in the North Atlantic was a bit low, albeit within a standard deviation of the historical annual mean. However, there is no indication of a systematic trend in MOC transport.
- Annual mean SLA was above the 1993–99 baseline average for nearly 80% of the ocean. The global mean SLA change of +6 mm from 2005 was the highest increase since the altimeter record began in 1993. Relative sea level change was also the highest ever recorded. There were an anomalously high number of extreme sea level events.
- Global ocean carbon uptake in 2005 (about 2.2 Pg C yr^{-1}) was near average for the past decade. Interannual variability over the past decade has been about $\pm 0.2 \text{ Pg C yr}^{-1}$. Atlantic Ocean anthropogenic CO_2 uptake continues to exceed Pacific Ocean uptake.
- Global annual average ocean color anomalies were not markedly different from those observed in the satellite record over the past decade. However,